Emergent Simplicities in Stochastic Intergenerational Homeostasis

Kunaal Joshi,[1†*] Charles S. Wright,[1†*] Karl F. Ziegler,[1†]
Elizabeth M. Spiers,[1] Jacob T. Crosser,[1] Samuel Eschker,[1]
Rudro R. Biswas,[1*] Srividya Iyer-Biswas[1,2*]

[1]Department of Physics and Astronomy, Purdue University, West Lafayette, Indiana, USA
[2]Santa Fe Institute, Santa Fe, NM 87501, USA

[†]These authors contributed equally to this work.
[*]Corresponding authors. Email: joshi84@purdue.edu, wrightcs@purdue.edu, rrbiswas@purdue.edu, iyerbiswas@purdue.edu.

Biological systems are complex and hierarchical, with inherent stochasticity of constitutive molecular processes. Yet, key physiological "state" variables are held in homeostasis. To identify quantitative rules governing the responsible control systems, we reconceptualize homeostasis as a dynamical—albeit stochastic—process, focusing on cell size homeostasis as a case study. Using our SChemostat technology, we obtain high-precision multigenerational trains of statistically identical, non-interacting individual bacterial cell sizes in well-defined environments. We first establish that individual cells indeed maintain stochastic intergenerational size homeostasis. Through extensive analysis of experimental data from multiple growth conditions, we uncover hidden simplicities including an intergenerational scaling law governing fluctuations in cell sizes across generations. These "emergent simplicities" place strong con-

straints on the dynamics: they specify, without fitting parameters, the precise stochastic map for the intergenerational evolution of cell sizes. Importantly, we find that intergenerational cell size homeostasis is achieved through reflexive, elastic adaptation. Thus, under balanced growth conditions, cell size cannot serve as a repository of intergenerational memory.

Homeostasis describes a self-regulating process wherein a complex system maintains internal stability despite unavoidable fluctuations in its constitutive dynamics. This concept was instrumental to the development of the field of physiology (*1*); as formulated by Bernard, stability of an organism's "internal milieu" is not simply a feature, but indeed a prerequisite for life (*2*). Early conceptualizations philosophically permitted the possibility of stochasticity in the homeostatic variable (*2–4*). However, deterministic frameworks have since become pervasive, with organisms thought—in analogy to mechanical self-regulating apparatuses—to defend the setpoint values of homeostatic variables (*5*) against intrinsic and extrinsic fluctuations. This approach can be traced to early developments in control theory as applied to engineered inanimate systems (*6*). Within this perspective, deviations from desired setpoints are taken to indicate organismal malfunction, rather than natural variability resulting from inherent stochasticity in the dynamics (*7, 8*).

Realistically, biological systems feature layered architectures and hierarchical organization, which must somehow conspire to ensure homeostasis of emergent organismal "state variables" despite the inherently probabilistic nature of the underlying biophysical dynamics (*1*). Embracing this systems design point of view, we conceptualize homeostasis as a dynamical—albeit stochastic—process, rather than as an end state (i.e., a setpoint). We further define the problem of stochastic homeostasis by distinguishing two potential routes to achieving it. We term the first option "elastic adaptation", a passive mechanism that involves reflexive responses to instantaneous conditions with no retention of long-term memory (as in Ashby's Homeostat (*9*), the first technical model of homeostasis). In contrast, active, "plastic adaptation" is achieved through reflective responses involving strategic integration over a finite memory of past fluctuations, which is accomplished by coordination between controller and sensor modules (as in Shannon's Maze Machine (*10*)). Which scheme(s) do organisms use?

To identify the quantitative principles that ensure the robust and dynamical control of stochas-

tic yet homeostatic organismal state variables, we turn to one of the simplest organisms—a bacterial cell—and one of its best-studied homeostatic state variables—cell size. Under optimal growth conditions, a single bacterial cell continuously undergoes growth and division, both inherently stochastic processes with significant fluctuations, yet maintains a typical size for a given environment (Fig. 2).

Current models of cell size homeostasis, informed by a wealth of single-cell datasets, typically build on the setpoint perspective and focus on specific hypothesized paradigms, pithily described as sizer, timer, and adder (*11–16*). These approaches use a deterministic lens to build a framework that describes specific intragenerational phenomenology, and thence formulate a quasi-deterministic heuristic to motivate the requirement that cell size homeostasis be achieved intergenerationally. Data from related bacterial species analyzed in the mother machine occupy distinct positions along the continuum between specific paradigms (*17*), although the preponderance of attention has focused on the adder paradigm as applied to model bacterial systems (*18–21*). Theoretical extrapolations of intergenerational dynamics based on observed intragenerational phenomenology are often used to identify which of these schemes most accurately describes how growth control is actualized in different microorganisms (*14, 21, 22*).

However, as immediately evident in the dramatic contrast between the quasi-deterministic framework's predictions (Fig. 1E) and high-precision single cell intergenerational data (Fig. 1F), these schemes may be unequivocally distinguished only in the deterministic case; in reality, homeostasis is an inherently stochastic process, whose study requires high-precision multigenerational datasets of statistically identical, non-interacting cells. A number of ingenious approaches have been developed to obtain single-cell datasets (*23–25*), but potential artifacts such as cell–cell contacts and differential nutrient diffusion (*26*) reduce the precision in control over growth conditions that each cell experiences. Because our SChemostat technology (*27*) addresses each of these concerns, we used it to capture high-precision datasets of statistically

identical, non-interacting *Caulobacter crescentus* cells over long periods of time (Fig. 1, A to D), demonstrating that multigenerational trains of sizes of individual cells deviate dramatically from the naïve predictions derived from these frameworks (Figs. 1-E and -F and Figs. S1, S2, and S3). Evidently, variations from the putative homeostatic setpoint are not only normal, but in fact an integral feature of the stochastic intergenerational homeostasis of an individual cell!

Taking a first principles-based approach deeply compatible with the underlying stochasticity, we previously observed remarkably precise intragenerational scaling laws ("emergent simplicities") in single-cell growth between successive division events, including collapse of the mean-rescaled distributions of intragenerational cell size and of interdivision times from different conditions onto universal curves (*28*). However, as these intragenerational scaling laws do not guarantee intergenerational homeostasis, we sought to characterize the phenomena of stochastic growth and division over many generations, without recourse to *a priori* assumptions about the machinery responsible for homeostasis.

Direct evidence of stochastic intergenerational homeostasis of individual bacterial cell sizes: Surprisingly, direct evidence for stochastic intergenerational cell-size homeostasis is not readily available in published works (*11–21*). Any attempt to confirm this hypothesis must meet both the necessary condition that mean cell size, averaged over an asynchronous population in balanced growth, be constant, as well as the sufficient condition that the distribution of cell sizes at birth ("initial size distribution") be time-invariant. Here, we present individual-cell multigenerational SChemostat data from three different balanced growth conditions: cells grown in complex (undefined) media, minimal (defined) media, and dilute complex media. By experimentally confirming both the necessary and sufficient conditions (Figs. 2, S6, and S5) we provide direct evidence of stochastic intergenerational homeostasis of individual cells.

Stochastic intergenerational cell size homeostasis is achieved through elastic adaptation: By analyzing successive values of initial cell size, we directly show that the intergenerational cell size dynamics are Markovian. Briefly, given a specified generation's initial size (a_1), the distribution of the next generation's initial size (a_2) is completely determined and does not depend on the preceding generations' initial sizes (a_0, a_{-1}, and so on) [Figs. S7, S8, and S9, and supplementary materials (SM), mathematical derivations section 1]. In other words, $P(a_n|a_{n-1}, a_{n-2}, a_{n-3}\ldots) = P(a_n|a_{n-1}) = P_1(a_n|a_{n-1})$ for any n under balanced growth conditions. This result is key to building the intergenerational theoretical framework. The immediate implication is that, under balanced growth conditions, intergenerational cell size homeostasis is maintained through reflexive, elastic adaptation. Surprisingly, under these conditions, cell size does not serve as a repository of intergenerational memory!

Theoretical formulation of stochastic intergenerational framework for cell size homeostasis: Using the key emergent simplicity that the intergenerational cell size dynamics are Markovian, the basic equation governing the multigenerational dynamics of initial cell sizes (SM, mathematical derivations section 2, and (*29*)) is:

$$P_n(a_n|a_0) = \left[\int_{-\infty}^{\infty}\right]^{n-1} \left[P_1(a_n|a_{n-1}) \prod_{j=1}^{n-1} \{P_1(a_j|a_{j-1}) da_j\}\right]. \tag{1}$$

In this formulation, homeostasis is achieved if $P_n(a_n|a_0)$ converges to the same well-behaved distribution for all values of initial cell sizes, a_0, after a sufficient number of generations ($n \gg 1$) have elapsed. This is indeed true for our data in all three conditions (Fig. 4).

Emergent simplicity: A scaling law governing stochastic intergenerational homeostasis: We then extracted from our data the conditional probability distribution of the final size conditioned on the initial size within the same generation, $P_f(a_f|a_i)$, and found a remarkable emergent simplicity (Fig. 3): the mean-rescaled distribution is independent of the value of the initial

size. Thus,

$$P_f(a_f|a_i) = \frac{1}{\mu_f(a_i)}\Pi_f\left(\frac{a_f}{\mu_f(a_i)}\right), \tag{2}$$

where Π_f is the mean-rescaled distribution with unit mean and $\mu_f(a_i) = \langle a_f|a_i\rangle$ is the mean of the final area, a_f, as a function of the initial area, a_i. This observation holds for all three conditions. This emergent simplicity facilitates our task of developing the theory of stochastic intergenerational homeostasis; instead of considering $P_f(a_f|a_i)$, which is generally a function of two variables, we need only work with two one-dimensional functions, Π_f and μ_f. Of these, $\mu_f(a_i)$ simply serves as a "calibration curve" for restoring the unscaled distribution from the universal mean-rescaled distribution for a given growth condition. From data, $\mu_f(a_i)$ is well approximated by a straight line (Fig. S11).

The exact stochastic map governing intergenerational cell size dynamics and homeostasis is directly validated by fitting-free data–theory comparisons: Taken together, these two emergent simplicities—the Markovian nature of intergenerational cell size dynamics (Figs. S7, S8, and S9) and the intergenerational scaling law (Eq. 2)—serve as starting points to motivate and develop a data-informed theoretical framework. Furthermore, these data reveal yet another emergent simplicity: the division ratio, r, defined as the ratio of the initial size in a given generation to the final size in the previous generation, is independent of the final size in the previous generation (Fig. S10; SM, mathematical derivations section 1, and (*29*)). Thus, $P(r|a_f) = P(r)$ is independent of a_f; when combined with Eq. (2), this implies that the conditional distribution of the next generation's initial size, conditioned on the current generation's initial size, must also undergo a scaling collapse upon rescaling by the conditional mean:

$$P_1(a_{n+1}|a_n) = \frac{1}{\mu(a_n)}\Pi\left(\frac{a_{n+1}}{\mu(a_n)}\right), \tag{3}$$

where Π denotes the new mean-rescaled distribution (with unit mean) and $\mu(a_n) = \langle a_{n+1}|a_n\rangle$ the conditional mean of the initial size in the next generation, given the initial size in the current generation. These functions can be related to the corresponding quantities in Eq. (2): $\Pi(s) = \langle r^{-1}\Pi_f(s\langle r\rangle/r)\rangle_r \langle r\rangle$ and $\mu(a) = \langle r\rangle \mu_f(a)$, where $\langle r\rangle$ is the mean division ratio and $\langle\cdot\rangle_r$ denotes averaging over fluctuations of r. We see direct evidence of this intergenerational scaling of initial sizes for all three conditions (Fig. S10).

Using this intergenerational scaling law and the Markovian framework in Eq. (1), we can predict the complete stochastic map for intergenerational cell size statistics of an individual cell in a given balanced growth condition, using as inputs the universal mean-rescaled distribution function, Π, and the calibration curve corresponding to the conditional mean, μ, for that growth condition (SM, mathematical derivations section 3, and (*29*)). Our fitting-free predictions match our data remarkably well for all conditions (Fig. 4). Thus, we have written down a data-validated fitting-free theoretical framework: the stochastic map governing stochastic intergenerational homeostasis! In (*29*), we show that our theoretical framework also accurately predicts the stochastic intergenerational cell size dynamics of *E. coli* and *B. subtilis* using published datasets (*13*). Although these species can undergo multifork replication under favorable conditions and obey additional constraints (*30*) that may not apply to *C. crescentus*, their cell size dynamics leading to stochastic intergenerational homeostasis are also governed by the theoretical framework we report here.

Stochasticity specifies the conditions for homeostasis: In addition to fully determining the stochastic map governing intergenerational homeostasis, the observed intergenerational scaling law also determines the general necessary and sufficient conditions for stochastic homeostasis: given the observed linear form of the conditional mean, $\mu(a) = \alpha a + \beta$, the magnitude of the slope, α, must be less than or equal to $1/s_{\text{max}}$, where s_{max} is the maximum allowed value of the

variable governed by the mean-rescaled probability distribution Π in Eq. (3) (see (*29*) for details of derivation). Conversely, given α, the upper bound of the Π distribution has to lie below $1/\alpha$. This prediction is indeed consistent with our data: the values of $1/\alpha$ corresponding to Figs. S10-B, -D and -F are $\sim 1.6, 1.5$ and 1.7, obtained from Figs. S11-B, -E and -H respectively. In each case, the mean-rescaled distribution is evidently bounded within corresponding value of $1/\alpha$.

Since Π has unit mean, the presence of stochasticity implies that $s_{\text{max}} > 1$; thus, our homeostasis requirement, $|\alpha| \leq 1/s_{\text{max}}$, is a stronger bound on α than that obtained from the quasi-deterministic sizer–timer–adder paradigm: $|\alpha| < 1$ (*18, 31–33*).

Reconciling the sizer–timer–adder framework with stochastic intergenerational dynamics: Combining our intergenerational framework with the linear nature of the conditional mean, we find that, given a starting cell size not equal to the homeostatic mean size, this cell's mean size in subsequent generations relaxes exponentially to the homeostatic mean size, with an exponential rate given by $\ln(1/|\alpha|)$ (as derived in (*29*)). A consequence is that the correlation function C_{mn} of cell sizes in generations m and n is also an exponential function with rate $\ln(1/|\alpha|)$ (SM, mathematical derivations section 4):

$$C_{mn} \propto \alpha^{|m-n|} = e^{-|m-n|\ln(1/\alpha)}. \tag{4}$$

Figs. S11-C, -F, and -I show good agreement between this theoretical prediction and the experimentally calculated correlation functions. This mean-level behavior is reminiscent of the quasi-deterministic evolution of cell size with generation, which is predicted to exponentially relax to the setpoint size with the same exponential rate, $\ln(1/|\alpha|)$ (Fig. S4). Thus, the quasi-deterministic picture describes an *average* cell, but not a *representative* cell (*34*).

Connections to the general homeostasis problem: Here we used the bacterial cell size homeostasis problem as a valuable case study to directly grapple with the inherently stochas-

tic and dynamic nature of homeostasis in living systems. In contrast to the typical approach, which starts from a deterministic point of view and adds "noise on top" to construct ad hoc quasi-deterministic frameworks motivated by analytic or computational tractability (rather than empirical observation), we retained the fully stochastic aspect of the problem at every stage of its conceptualization and description, ultimately formulating a first principles-based analytic theory with spectacular fitting-free data–theory matches. These results specify the exact stochastic map governing stochastic intergenerational cell-size homeostasis, thus determining the necessary and sufficient condition for stochastic homeostasis; in addition, they accurately determine the dynamics of intergenerational homeostasis of other microorganisms for which data are available (*29*). Finally, they reinforce the insight that the mythical "average cell" described by the deterministic limit fundamentally fails to capture the true behaviors of the typical individual cell that experiences stochastic homeostasis (*34*).

Our approach of identifying "top down" organism-level emergent simplicities complements the common atomistic view that understanding essentially complex phenomena in essentially complex systems, such as whole organisms, must focus on the dissection of genetic and signaling networks (*35*). Our results transcend the minutiae of the condition-specific molecular networks implicated in growth control in distinct environmental conditions and organisms. The intergenerational scaling law holds across multiple balanced growth conditions, and across multiple bacterial species. However, the shape of the collapsed distribution changes from condition to condition. The mechanism is universal, but the specific instantiation depends on the characteristics of the balanced growth condition. Intriguingly, the data presented here show early indications of a "precision–speed" tradeoff (*36*), encapsulated in the different shapes of the mean-rescaled curves from different growth conditions—narrower for the slower growth condition (defined minimal media) and broader for the faster growth condition (undefined complex media). An analogous precision–energy tradeoff is indicated in the observation that the slope,

α, of the mean calibration curve, $\mu(a_i) = \alpha a_i + \beta$, is comparatively closer to the *upper* limit $1/s_{\text{max}}$ set by our intergenerational framework, and not a lower value such as 0 that would correspond to perfect size control. What costs and benefits would determine the tradeoffs and optima in these contexts? These promising lines of future inquiry build on the results presented here.

Despite the long-standing criticism directed at the simplicity of the memory-free design of Ashby's Homeostat, our work shows it to be a representative model for natural homeostasis in a living organism, after all! Perhaps this is the most startling and elegant simplicity uncovered: over intergenerational timescales, cell size homeostasis is an elastically adapting process. While excitement has been building around the general possibility that single cells may serve as useful arenas for exploring the phenomenology of learning without neurons (*37, 38*), our work shows that bacterial cell size, under balanced growth conditions, is not a repository of cellular memory and therefore cannot serve as a diffuse living brain with a capacity for learning on intergenerational timescales. Where then is a bacterial cell's intergenerational memory encoded? Early indications are that the instantaneous single-cell growth rate may be the answer (*39, 40*).

References

1. G. E. Billman, *Frontiers in Physiology* **11** (2020).

2. C. Bernard, *Introduction à l'étude de la médecine expérimentale*, no. 2 (JB Baillière, 1865).

3. W. B. Cannon, *À Charles Richet: ses amis, ses collègues, ses élèves (in French)*, A. Pettit, ed. (Les Éditions Médicales, Paris, 1926), p. 91.

4. W. B. Cannon, *The Wisdom of the Body* (W.W. Norton & Company, Inc., New York, 1932).

5. J. D. Hardy, *Harvey Lectures* **49**, 242 (1953–1954).

6. N. Wiener, *Cybernetics: or Control and Communication in the Animal and the Machine* (MIT Press, Cambridge, MA, 1948).

7. M. E. Kotas, R. Medzhitov, *Cell* **160**, 816 (2015).

8. S. Mukherjee, *The Song of the Cell: An Exploration of Medicine and the New Human* (Simon and Schuster, 2022).

9. W. R. Ashby, *Radio Electronics* pp. 77–79 (March Issue, 1949).

10. *Life Magazine* **33**, 45 (1952).

11. T. W. Spiesser, C. Müller, G. Schreiber, M. Krantz, E. Klipp, *The FEBS Journal* **279**, 4213 (2012).

12. M. Deforet, D. van Ditmarsch, J. B. Xavier, *Biophysical Journal* **109**, 521 (2015).

13. S. Taheri-Araghi, *et al.*, *Current Biology* **25**, 385 (2015).

14. J. T. Sauls, D. Li, S. Jun, *Current Opinion in Cell Biology* **38**, 38 (2016).

15. M. M. Logsdon, *et al.*, *Current Biology* **27**, 3367 (2017).

16. L. Willis, K. C. Huang, *Nature Reviews Microbiology* **15**, 606 (2017).

17. S. Jun, S. Taheri-Araghi, *Trends in Microbiology* **23**, 4 (2015).

18. A. Amir, *Physical Review Letters* **112**, 208102 (2014).

19. M. Campos, *et al.*, *Cell* **159**, 1433 (2014).

20. J. Lin, A. Amir, *Cell Systems* **5**, 358 (2017).

21. F. Si, *et al.*, *Current Biology* **29**, 1760 (2019).

22. K. R. Ghusinga, C. A. Vargas-Garcia, A. Singh, *Scientific Reports* **6**, 30229 (2016).

23. P. Wang, *et al.*, *Current Biology* **20**, 1099 (2010).

24. J. R. Moffitt, J. B. Lee, P. Cluzel, *Lab on a Chip* **12**, 1487 (2012).

25. T. M. Norman, N. D. Lord, J. Paulsson, R. Losick, *Nature* **503**, 481 (2013).

26. L. Potvin-Trottier, S. Luro, J. Paulsson, *Current Opinion in Microbiology* **43**, 186 (2018).

27. S. Iyer-Biswas, *et al.*, *Proceedings of the National Academy of Sciences of the United States of America* **111**, 15912 (2014).

28. S. Iyer-Biswas, G. E. Crooks, N. F. Scherer, A. R. Dinner, *Physical Review Letters* **113** (2014).

29. K. Joshi, R. R. Biswas, S. Iyer-Biswas, *bioRxiv:2023.01.20.525000* (2023).

30. M. Scott, T. Hwa, *Current Opinion in Biotechnology* **22**, 559 (2011).

31. L. Susman, *et al.*, *Proceedings of the National Academy of Sciences of the United States of America* **115**, E5679 (2018).

32. W. F. Marshall, *Annual Review of Biophysics* **45**, 49 (2016).

33. M. B. Ginzberg, R. Kafri, M. Kirschner, *Science* **348**, 1245075 (2015).

34. S. Sanders, K. Joshi, P. A. Levin, S. Iyer-Biswas, *PLoS Genetics* **19**, e1010505 (2023).

35. L. H. Hartwell, J. J. Hopfield, S. Leibler, A. W. Murray, *Nature* **402**, C47 (1999).

36. G. Lan, P. Sartori, S. Neumann, V. Sourjik, Y. Tu, *Nature Physics* **8**, 422 (2012).

37. J. Gunawardena, *Proceedings of the IEEE* **110**, 590 (2022).

38. D. Rajan, *et al.*, *Current Biology* **33**, 241 (2023).

39. K. Joshi, *et al.*, *bioRxiv:2023.05.27.542601* (2023).

40. K. Joshi, S. Roy, R. R. Biswas, S. Iyer-Biswas, *bioRxiv:10.1101/2023.03.07.531540* (2023).

41. F. Jafarpour, *et al.*, *Physical Review X* **8**, 021007 (2018).

42. C. S. Wright, *et al.*, *Scientific Reports* **5**, 9155 (2015).

Acknowledgments

S.E. and S.I.-B thank Purdue's Data Mine Learning Community for computational resources. We are grateful to the Iyer-Biswas group members for insightful discussions and feedback. S.I.-B. thanks Daniel S. Fisher for useful questions.

Funding: K.J. and S.I.-B. acknowledge support from the Ross-Lynn Fellowship award. We thank Purdue University Startup funds, Purdue Research Foundation, the Purdue College of Science Dean's Special Fund, and the Showalter Trust for financial support.

Author contributions: K.J. and S.I.-B. conceived of the research; K.J., R.R.B. and S.I.-B. designed the research; K.J. extracted the intergenerational scaling law from the data and performed data analysis under the guidance of S.I.-B.; K.J., R.R.B. and S.I.-B. developed the theoretical framework and performed analytic calculations; C.S.W. and S.I-.B. designed the experimental setup; C.S.W. and K.F.Z. actualized and refined the experimental pipeline under the guidance of S.I.-B.; C.S.W. and S.E. designed and developed the analysis pipeline with input from R.R.B. and S.I.-B.; C.S.W, K.F.Z., E.S., J.C. and S.I.-B. performed experiments; K.J., C.S.W., R.R.B. and S.I.-B. wrote the paper with input from all authors; S.I.-B. supervised the research.

Competing interests: The authors declare that they have no competing interests.

Supplementary Materials

Materials and Methods

Mathematical Derivations

Figs. S1 to S11

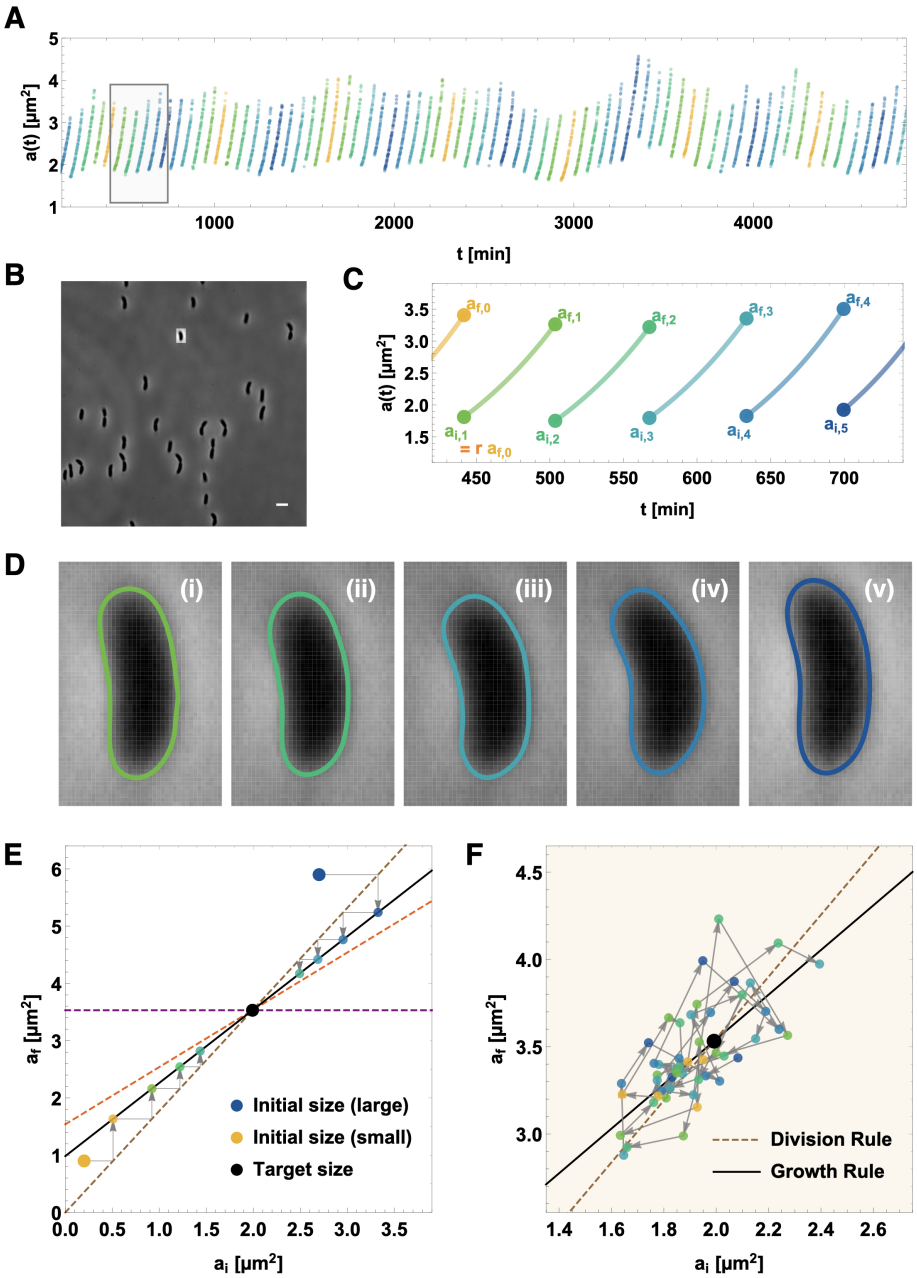
A
a(t) [μm²]
t [min]
B
C
a(t) [μm²]
t [min]
= r a_f,0
D
(i)
(ii)
(iii)
(iv)
(v)
E
a_f [μm²]
a_i [μm²]
Initial size (large)
Initial size (small)
Target size
F
a_f [μm²]
a_i [μm²]
Division Rule
Growth Rule

Fig. 1: **Stochastic intergenerational cell size trajectories of individual bacterial cells.** (**A**) A typical individual *C. crescentus* stalked cell's intergenerational growth and division trajectory obtained using our SChemostat technology under time-invariant balanced growth conditions. Colors indicate generations of the cell. (**B**) Representative experimental field of view, highlighting the cell corresponding to the trajectory in (A). Scale bar = 2 μm. (**C**) Exponential fits to growth trajectories of the generations corresponding to the box in (A), with initial size ($a_{i,n}$, size at birth) and final size ($a_{f,n}$, size at division) as indicated. The division ratio (r) relates $a_{i,n}$ to $a_{f,n-1}$. (**D**) Cell boundary splines generated by our custom automated image analysis routines, corresponding to $a_{i,n}$ in (C). (**E**) Geometric interpretation of the heuristic argument for intergenerational homeostasis in the quasi-deterministic sizer–timer–adder paradigms. Dashed lines relate a_f to a_i in the sizer (*purple*, null slope), timer (*brown*, null intercept), and adder (*orange*, unit slope) mechanisms. The timer coincides with the "division rule", which determines the size after division, $a_{i,n} = ra_{f,n-1}$. The solid line is the experimentally measured "growth rule", which allows the final size to be set by the initial size of the same generation. Cells deterministically adjusts their size to exponentially relax to the target size set by the intersection between the growth and division rules. (**F**) Representative trajectory calculated directly from our high-precision single-cell experimental observations showing stochastic intergenerational cell size homeostasis dynamics. Extensive sets of individual cell data as shown in (F) are given for all three balanced growth conditions in Figs. S1, S2, and S3.

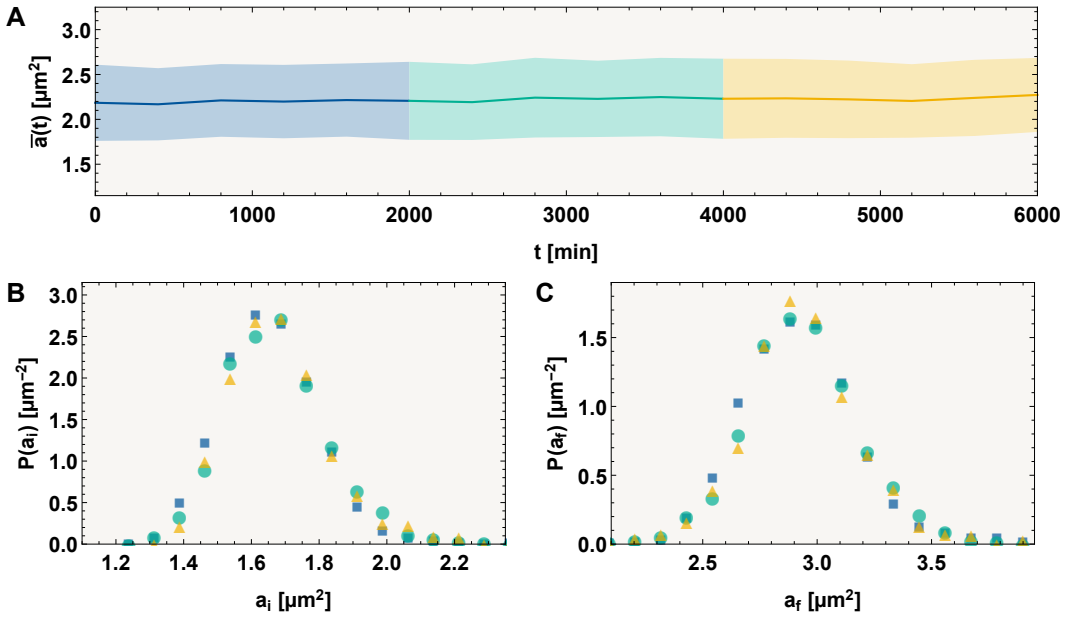

Fig. 2: **Precision measurements establish that individual cells maintain stochastic intergenerational cell size homeostasis.** (**A**) The mean cell size averaged over an asynchronous population in balanced growth remains invariant when cell size homeostasis has been attained. The distributions of pooled (**B**) initial cell size and (**C**) final cell size are plotted for cell generations drawn from the three time windows shown in (A), using corresponding colors. These distributions are invariant, establishing that stochastic intergenerational homeostasis has been achieved and is sustained. Corresponding figures for individual cells in other balanced growth conditions are shown in Figs. S5 and S6.

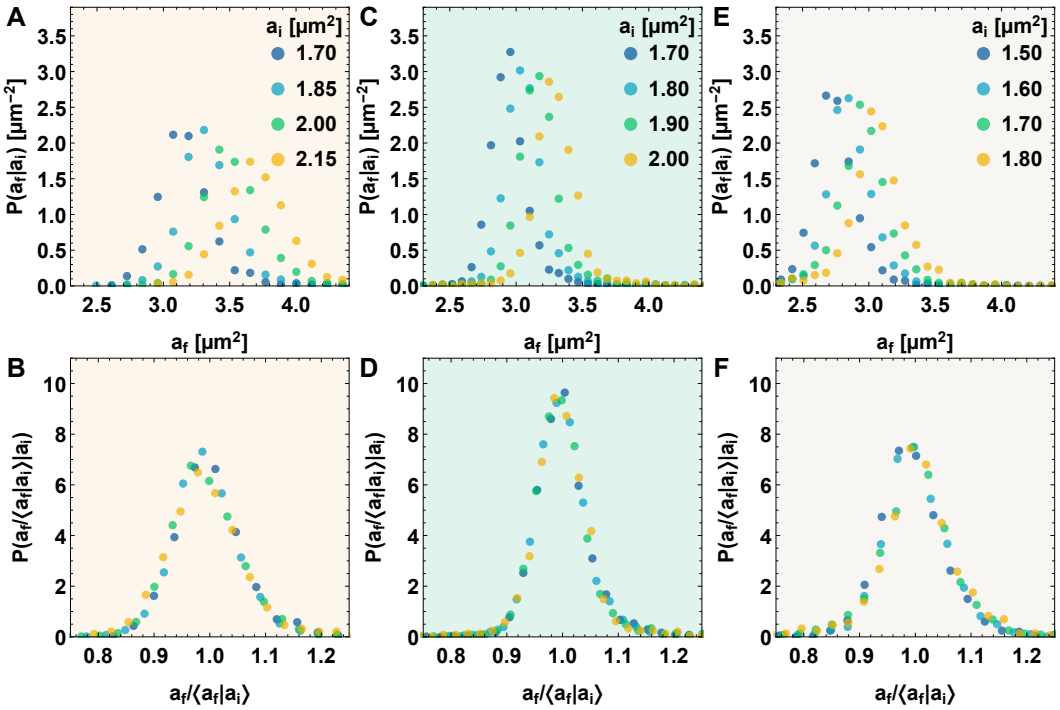

Fig. 3: **Emergent simplicity: intergenerational scaling law governing stochastic individual cell size homeostasis.** The top row shows $P_f(a_f|a_i)$, the distribution of final size, a_f, pooled by distinct values of initial size, a_i, within the same generation. Point colors indicate distinct values of a_i; background colors correspond to different growth media. The bottom row shows corresponding mean-rescaled distributions, with point and background colors as indicated in the top row. Here, $\langle a_f|a_i\rangle = \mu_f(a_i)$ is the mean a_f for a given a_i. These mean-rescaled distributions, while independent of initial size values, a_i, can differ in shape from one growth condition to another. Thus, we have found an emergent simplicity: for a given growth condition, the two-dimensional function $P_f(a_f|a_i)$ is constructed from two one-dimensional functions: the mean-rescaled distribution (bottom row), and the a_i-dependent mean $\mu_f(a_i)$, which sets the calibration curve for how to "stretch" the a_i-independent rescaled distributions (bottom row) to recover the a_i-dependent distributions (top row). Growth conditions are (**A** and **B**) complex media, (**C** and **D**) minimal media, and (**E** and **F**) dilute complex media.

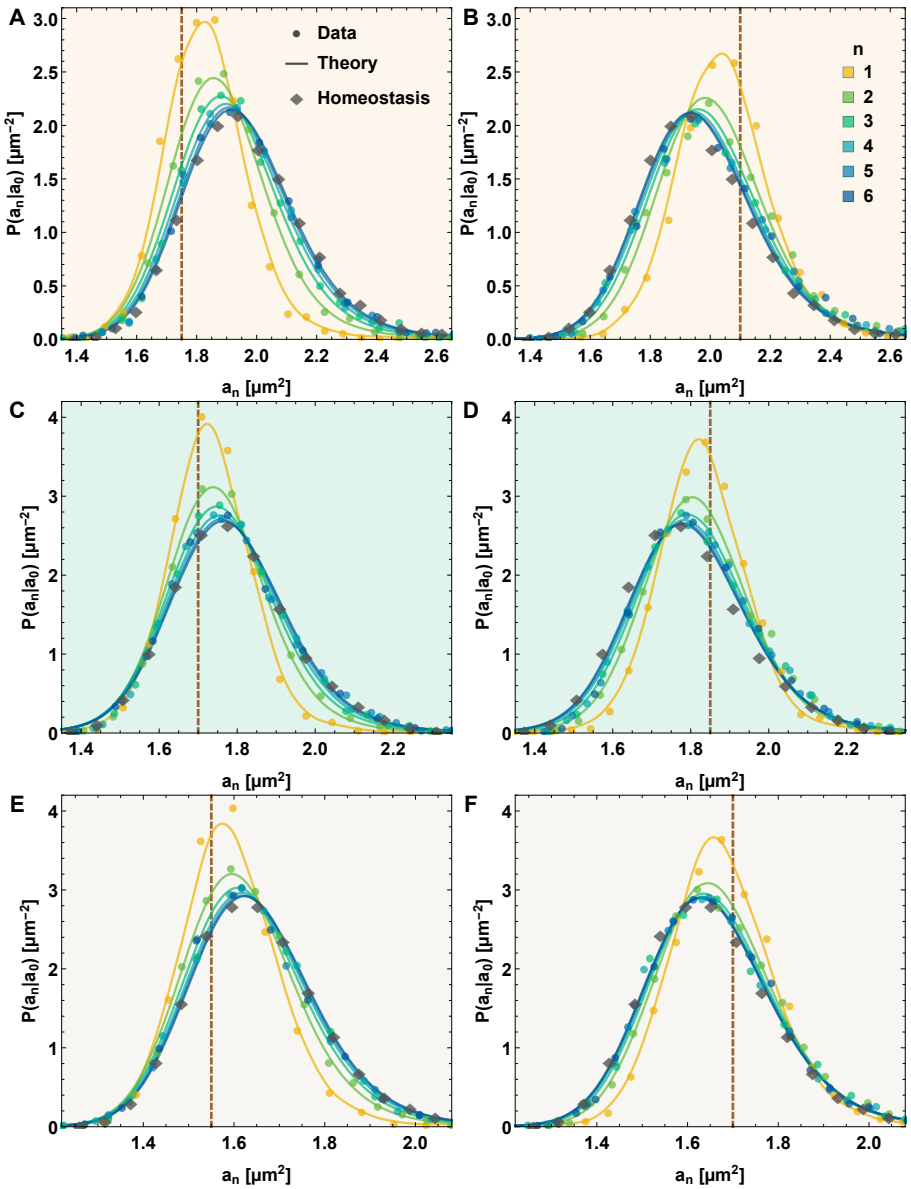
A
B
C
D
E
F
Data
Theory
Homeostasis
n
1
2
3
4
5
6
P(a_n|a_0) [μm^-2]
a_n [μm^2]

Fig. 4: **Our theoretical framework accurately predicts, with no fitting parameters, the size-by-size intergenerational cell size dynamics leading to stochastic homeostasis.** Each panel shows the intergenerational evolution of the distribution of initial cell sizes, a_i, starting from a given initial size in the starting generation (location of dashed line). n denotes the generation number, with the starting generation labeled by $n = 0$. Each row displays two different starting values of a_i for the same growth condition. Different rows correspond to different growth media, distinguished by background color. Points correspond to experimental data and curves to fitting-free predictions from our theoretical intergenerational framework, which takes as inputs the directly measured mean-rescaled distribution and mean calibration curve (Fig. S10 and Figs. S11-B, -E, and -H). The compelling fitting-free data–theory match independently validates the emergent simplicities used as inputs for our theoretical framework: the Markovian nature of intergenerational cell size dynamics and a_i-independence of the mean-rescaled size distribution. Growth conditions are (**A** and **B**) complex media, (**C** and **D**) minimal media, and (**E** and **F**) dilute complex media.

Materials and Methods

SChemostat imaging protocol: The conditionally adhesive *C. crescentus* strain IB001 was introduced into a single-channel microfluidic device and cells were incubated for one hour in the presence of the vanillate inducer, which promotes adhesion, as described in (*27, 41*). Growth medium was then infused through the channel at a constant flow rate of 10 µL/min (Pump 11 Elite, Harvard Apparatus) to flush out non-adherent cells and ensure continuous delivery of nutrients and removal of waste. Growth medium consisted of complex medium (peptone-yeast extract; PYE), dilute PYE, or minimal growth medium with xylose as sole carbon source (M2X). A microscope (Nikon Ti Eclipse with perfect focus system) and motorized XY stage (Prior Scientific ProScan III) under computerized control (LabVIEW 8.6, National Instruments) were used to acquire phase-contrast images at a magnification of 250X (EMCCD: Andor iXon+; objective: Nikon Plan Fluor 100X oil objective plus 2.5X expander; lamp: Prior LED). The microfluidic device, growth medium, and imaging apparatus were located inside a custom built acrylic microscope enclosure equilibrated to 30 °C (temperature controller: CSC32J, Omega and heater fan: HGL419, Omega); this chamber was in turn located within a sealed room with defined temperature and humidity to provide an additional level of environmental control. A typical experiment consists of tens of such fields of view, imaged tens of times between successive division events, with constant cell number and density for the duration of the experiment.

Image analysis: Image analysis to extract single-cell growth trajectories was conducted using custom-built Python software as described in (*27, 42*). Briefly, individual cells were identified in each phase-contrast image using a pixel-based edge detection routine, then the cell boundary was computed by interpolating a smoothing B-spline to the edge pixels. Full time series were constructed by tracking individual cells between frames. Automated image processing results were manually verified to ensure correct timing of every division event and to remove a small

fraction of data points with insufficient image quality to accurately determine cell size (e.g., resulting from a cell twisting out of the imaging plane, or from nearby cells touching). These boundaries are used to compute cell areas with $\mathcal{O}(1\%)$ measurement precision.

Mathematical Derivations

1. Notation: We use a_i to denote generic size at birth (initial size) and a_f to denote size at division (final size); a_n (where n is distinct from i or f) is a random number that denotes the initial size in the nth generation; $\hat{a}_n$ is a random number that denotes the final size at the end of the nth generation; r is a random number that is the division ratio, the ratio of the initial size to the final size in the previous generation, defined using the relation $a_{n+1} = r\hat{a}_n$; $P(X)$ is the usual notation denoting the probability distribution of random variable X; $P(X|Y)$ denotes the conditional probability distribution of X conditioned on Y; $\langle X|Y\rangle$ denotes the conditional average of X conditioned on Y; $P_f(a_f|a_i)$ denotes the probability distribution of a_f conditioned on a_i within the same generation; $P_n(a|a_0)$ is the probability distribution of a_n at a conditioned on a_0, the initial size in generation 0, often referred to as the (arbitrarily chosen) "initial" generation; and $P_r(r)$ denotes the probability distribution of the division ratio r in any generation, while $P_r(r|a_f)$ is the distribution of r conditioned on the corresponding final size a_f.

2. Derivation of intergenerational framework: Since in balanced growth conditions the sequence of initial cell sizes $a_0 \to a_1 \to \ldots \to a_n$ occurs through a Markov process (i.e., is a Markov chain), the probability distribution of the final generation size, a_n, can be expressed as a convolution of conditional probabilities governing each step in the sequence:

$$P_n(a_n|a_0) = \iint P_1(a_n|a_{n-1})da_{n-1}P_1(a_{n-1}|a_{n-2})da_{n-2} \times \ldots \times P_1(a_2|a_1)da_1P_1(a_1|a_0). \tag{S-1}$$

This is the same as Eq. (1) in the main text.

3. Relating the functions Π and μ to Π_f and μ_f: We begin with the emergent simplicity encapsulated in Eq. (2), expressed for initial and final sizes in generation n:

$$P_f(\hat{a}_n|a_n) = \frac{1}{\mu_f(a_n)}\Pi_f\left(\frac{\hat{a}_n}{\mu_f(a_n)}\right). \tag{S-2}$$

The initial size in the next generation, a_{n+1}, can be found from the final size, $\hat{a}_n$, in generation n, using the division ratio r: $a_{n+1} = r\hat{a}_n$. Given that r is a random variable with distribution $P_r(r)$ that is independent of $\hat{a}_n$, we can relate the mean of a_{n+1}, $\mu(a_n)$, to the mean of $\hat{a}_n$, $\mu_f(a_n)$, as follows:

$$\mu(a_n) = \langle\langle a_{n+1}\rangle\rangle_r = \langle\langle r\hat{a}_n\rangle\rangle_r = \langle r\rangle\,\langle\langle \hat{a}_n\rangle\rangle_r = \langle r\rangle\,\mu_f(a_n). \tag{S-3}$$

Note that there are two steps of averaging; the inner angular brackets average over possible growth-division processes at fixed r, whereas the outer angular brackets independently average over r). Meanwhile, the conditional probability distribution of a_{n+1} given a_n becomes:

$$\begin{aligned} P_1(a_{n+1}|a_n) &= \iint d\hat{a}_n dr P_r(r)\delta(a_{n+1} - r\hat{a}_n)P_f(\hat{a}_n|a_n) \\ &= \int dr P_r(r)\frac{1}{r}P_f\left(\frac{a_{n+1}}{r}|a_n\right). \end{aligned} \tag{S-4}$$

Herein, δ denotes the Dirac delta function. Using Eqs. (S-2) and Eq. (S-3),

$$\begin{aligned} P_1(a_{n+1}|a_n) &= \int dr P_r(r)\frac{1}{r}\frac{1}{\mu_f(a_n)}\Pi_f\left(\frac{a_{n+1}}{r\mu_f(a_n)}\right) = \left\langle \frac{\langle r\rangle}{r\mu(a_n)}\Pi_f\left(\frac{\langle r\rangle\, a_{n+1}}{r\mu(a_n)}\right)\right\rangle_r \\ &= \frac{\langle r\rangle}{\mu(a_n)}\left\langle \frac{1}{r}\Pi_f\left(\frac{\langle r\rangle}{r}\frac{a_{n+1}}{\mu(a_n)}\right)\right\rangle_r. \end{aligned} \tag{S-5}$$

We have thus arrived at the final intergenerational scaling form in the main text, Eq. (3), with the scaling function $\Pi(s)$ defined (setting $s = a_{n+1}/\mu(a_n)$ in the above) as:

$$\Pi(s) = \langle r\rangle\left\langle \frac{1}{r}\Pi_f\big(s\,\langle r\rangle/r\big)\right\rangle_r. \tag{S-6}$$

4. Deriving the correlation function, C_{mn}, from the mean: In balanced growth conditions with $\mu(a) = \alpha a + \beta$, when starting from an initial size a_0 (in generation 0) that is different from the homeostatic mean $\langle a \rangle_\infty$, the distributions of initial sizes in subsequent generations decay exponentially to the homeostatic mean with rate $\ln(1/\alpha)$:

$$\langle a_n - \langle a \rangle_\infty \rangle = (a_0 - \langle a \rangle_\infty)\, \alpha^n. \tag{S-7}$$

See (*29*) for details of the derivation. The angular brackets above denote a path average in a single cell. Since in balanced growth conditions generation 0 can be chosen arbitrarily, for $m > n$,

$$\langle a_m - \langle a \rangle_\infty \rangle = (a_n - \langle a \rangle_\infty)\, \alpha^{m-n}. \tag{S-8}$$

The steady state correlation function C_{mn} is calculated by performing both cell and population averages. Denoting the population average by $\langle \cdot \rangle_{\text{pop}}$ and assuming $m > n$,

$$\begin{aligned} C_{mn} &= \langle \langle (a_m - \langle a \rangle_\infty)\, ((a_n - \langle a \rangle_\infty)) \rangle \rangle_{\text{pop}} \\ &= \left\langle (a_n - \langle a \rangle_\infty)\, \alpha^{m-n}\, ((a_n - \langle a \rangle_\infty)) \right\rangle_{\text{pop}} \\ &= \left\langle (a_n - \langle a \rangle_\infty)^2 \right\rangle_{\text{pop}} \alpha^{m-n} = \text{Var}_\infty(a) \alpha^{m-n}. \end{aligned} \tag{S-9}$$

In the last step, $\text{Var}_\infty(a)$ is the generation-independent homeostatic variance of the size. When $m < n$, we exchange m and n in the expression, arriving at Eq. (4) in the main text.

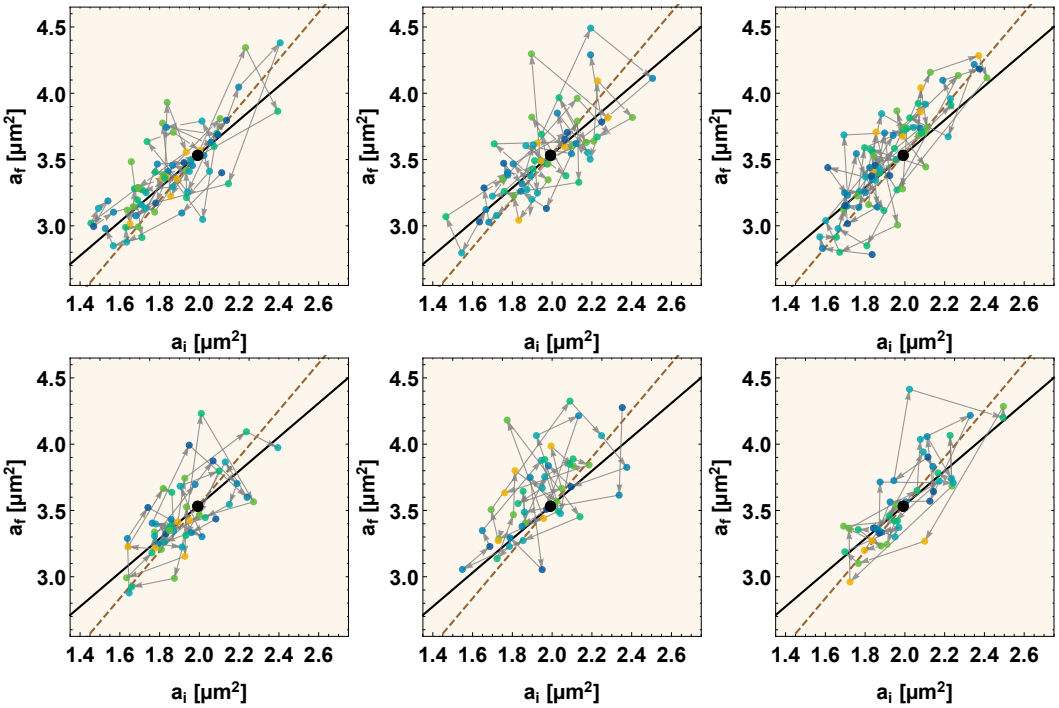

Fig. S1: **Representative single-cell intergenerational cell size trajectories calculated directly from our high-precision single-cell experimental observations in complex media.** Points corresponds to single generations, and relate initial and final cell sizes (a_i and a_f, respectively), within that generation. Successive generations are related by arrows. Each panel shows data from an individual cell. These progressions are dramatically different from the prevailing quasi-deterministic sizer–timer–adder paradigm. Stochasticity is integral to intergenerational cell size homeostasis dynamics; there is no resemblance to the deterministic approach to a target size as suggested in Fig. 1E. Representative single-cell trajectories are also provided for minimal media (Fig. S2) and dilute complex media (Fig. S3).

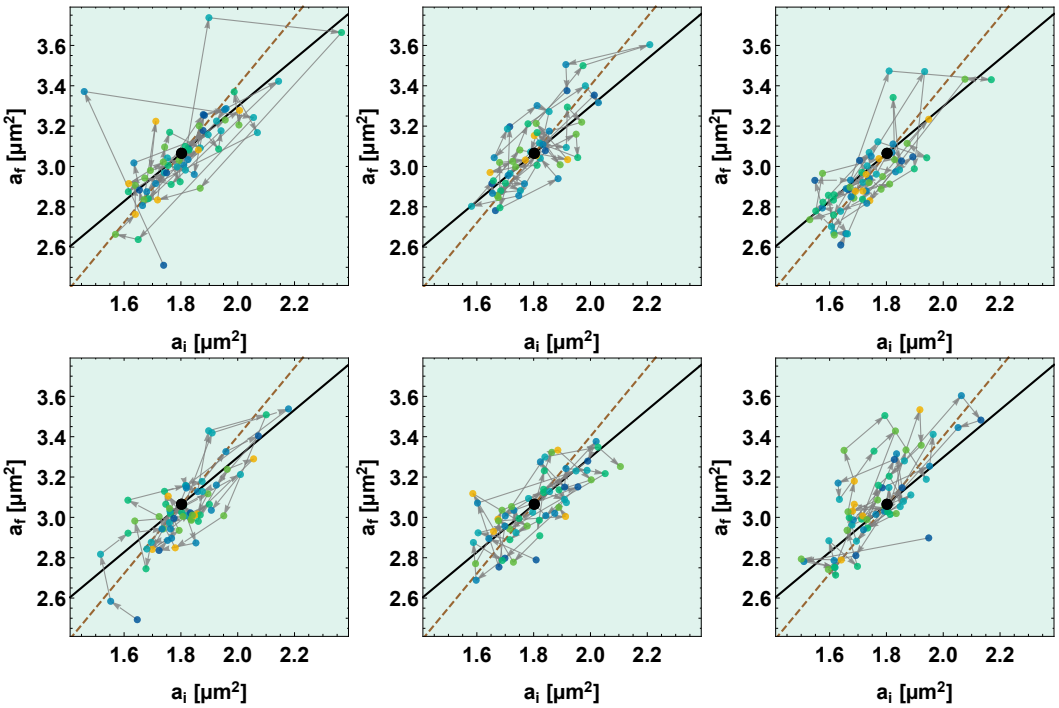

Fig. S2: **Representative single-cell intergenerational cell size trajectories calculated directly from our high-precision single-cell experimental observations in minimal media.** Points corresponds to single generations, and relate initial and final cell sizes (a_i and a_f, respectively), within that generation. Successive generations are related by arrows. Each panel shows data from an individual cell. These progressions are dramatically different from the prevailing quasi-deterministic sizer–timer–adder paradigm. Stochasticity is integral to intergenerational cell size homeostasis dynamics; there is no resemblance to the deterministic approach to a target size as suggested in Fig. 1E. Representative single-cell trajectories are also provided for complex media (Fig. S1) and dilute complex media (Fig. S3).

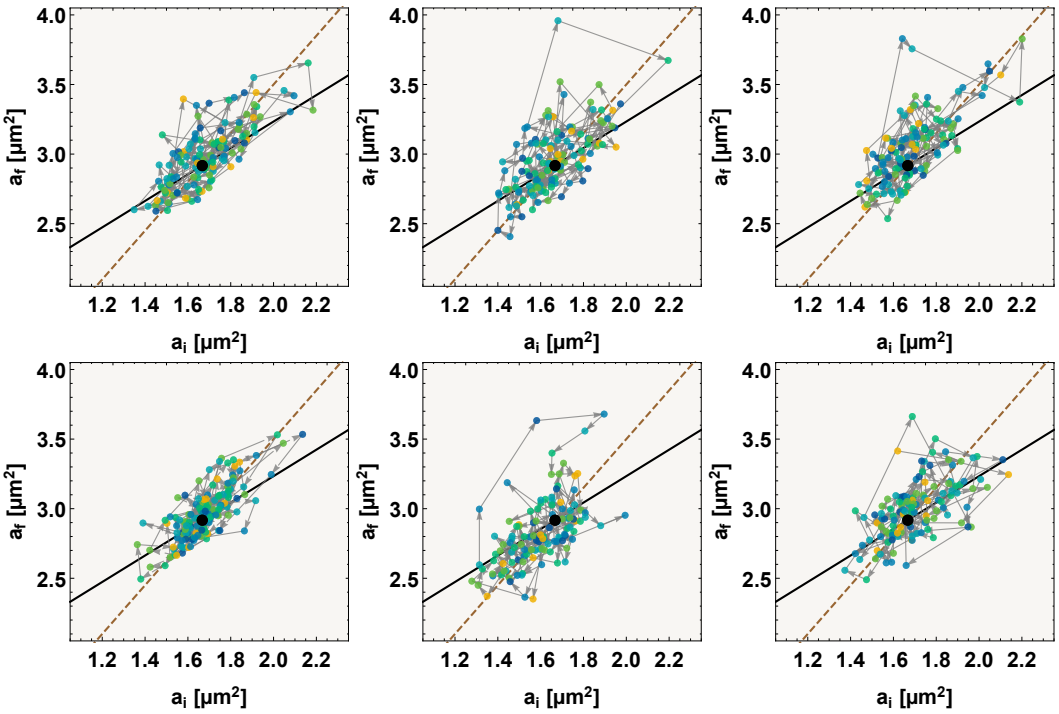

Fig. S3: **Representative single-cell intergenerational cell size trajectories calculated directly from our high-precision single-cell experimental observations in dilute complex media.** Points corresponds to single generations, and relate initial and final cell sizes (a_i and a_f, respectively), within that generation. Successive generations are related by arrows. Each panel shows data from an individual cell. These progressions are dramatically different from the prevailing quasi-deterministic sizer–timer–adder paradigm. Stochasticity is integral to intergenerational cell size homeostasis dynamics; there is no resemblance to the deterministic approach to a target size as suggested in Fig. 1E. Representative single-cell trajectories are also provided for complex media (Fig. S1) and minimal media (Fig. S2).

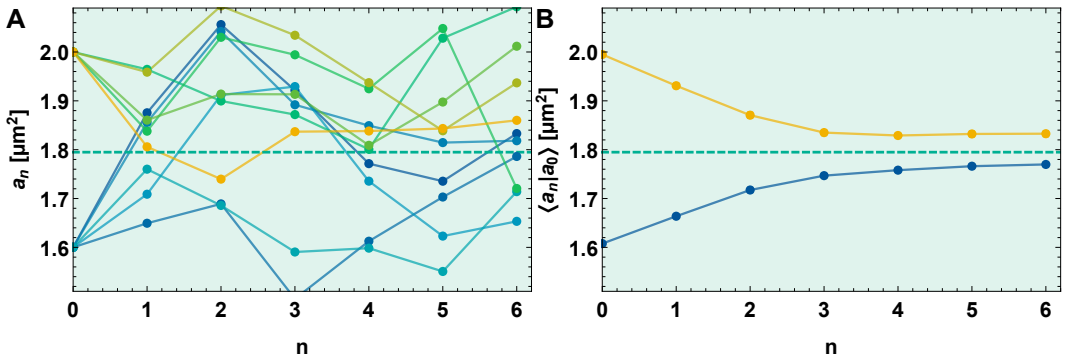

Fig. S4: **Experimental visualization of intergenerational homeostasis as achieved by actual single cells versus the mythical "average" cell.** Behavior of cells starting from given initial size. (**A**) Initial areas from five randomly selected trajectories over successive generations for cells starting from two different starting initial areas (1.6 and 2.0 μm^2, respectively). The dashed line represents the population mean of initial areas. (**B**) Mean initial areas across successive generations that start from the same initial areas as in (A). Although the trajectories of individual cells (A) do not follow a pattern discernible by eye, their mean (B) converges to the population mean following the calibration curve of $\langle a_1|a_0\rangle$ in Fig. S11E.

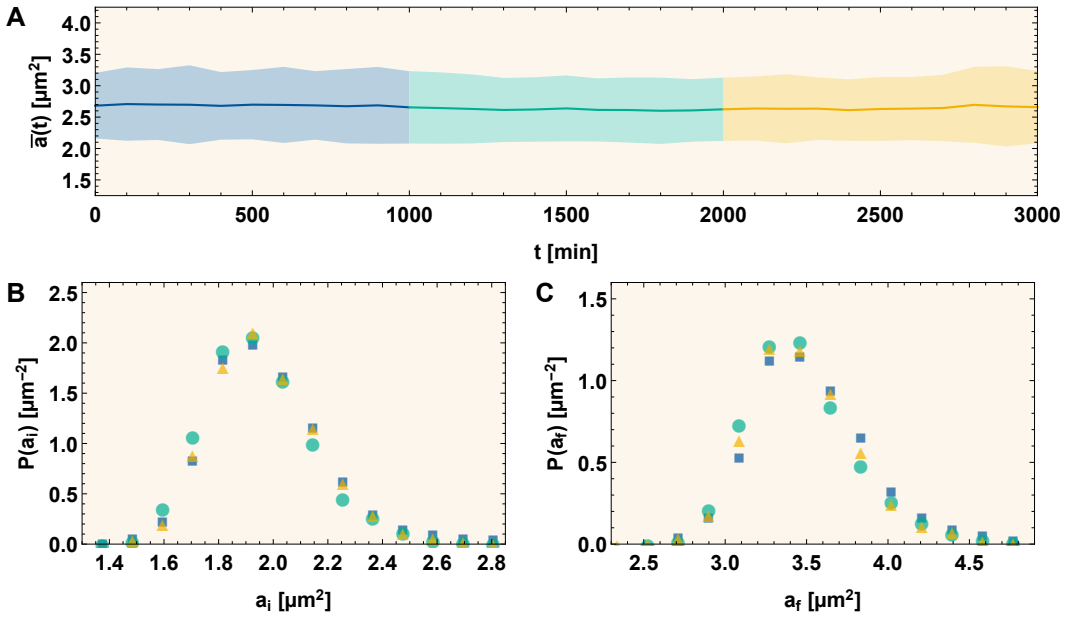

Fig. S5: **Precision measurements establish that individual cells maintain stochastic intergenerational cell size homeostasis in complex media.** (**A**) The mean cell size averaged over an asynchronous population in balanced growth remains invariant when cell size homeostasis has been attained. The distributions of pooled (**B**) initial cell size and (**C**) final cell size are plotted for cell generations drawn from the three time windows shown in (A), using corresponding colors. These distributions are invariant, establishing that stochastic intergenerational homeostasis has been achieved and is sustained. Corresponding figures for individual cells in balanced growth conditions are provided for dilute complex media (Fig. 2) and minimal media (Fig. S6).

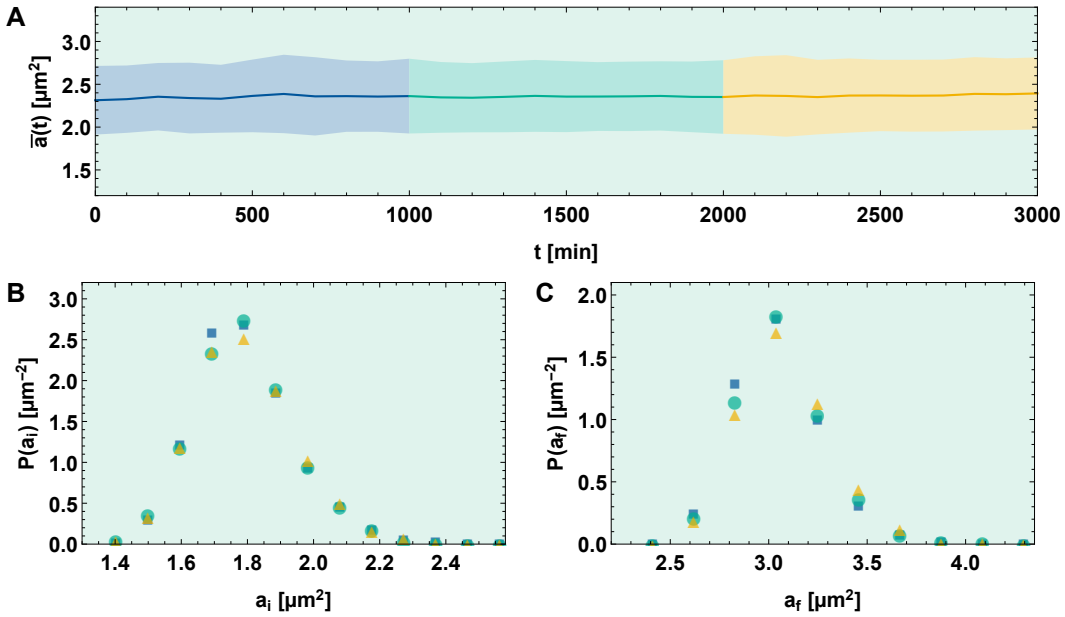

Fig. S6: **Precision measurements establish that individual cells maintain stochastic intergenerational cell size homeostasis in minimal media.** (**A**) The mean cell size averaged over an asynchronous population in balanced growth remains invariant when cell size homeostasis has been attained. The distributions of pooled (**B**) initial cell size and (**C**) final cell size are plotted for cell generations drawn from the three time windows shown in (A), using corresponding colors. These distributions are invariant, establishing that stochastic intergenerational homeostasis has been achieved and is sustained. Corresponding figures for individual cells in balanced growth conditions are provided for dilute complex media (Fig. 2) and complex media (Fig. S5).

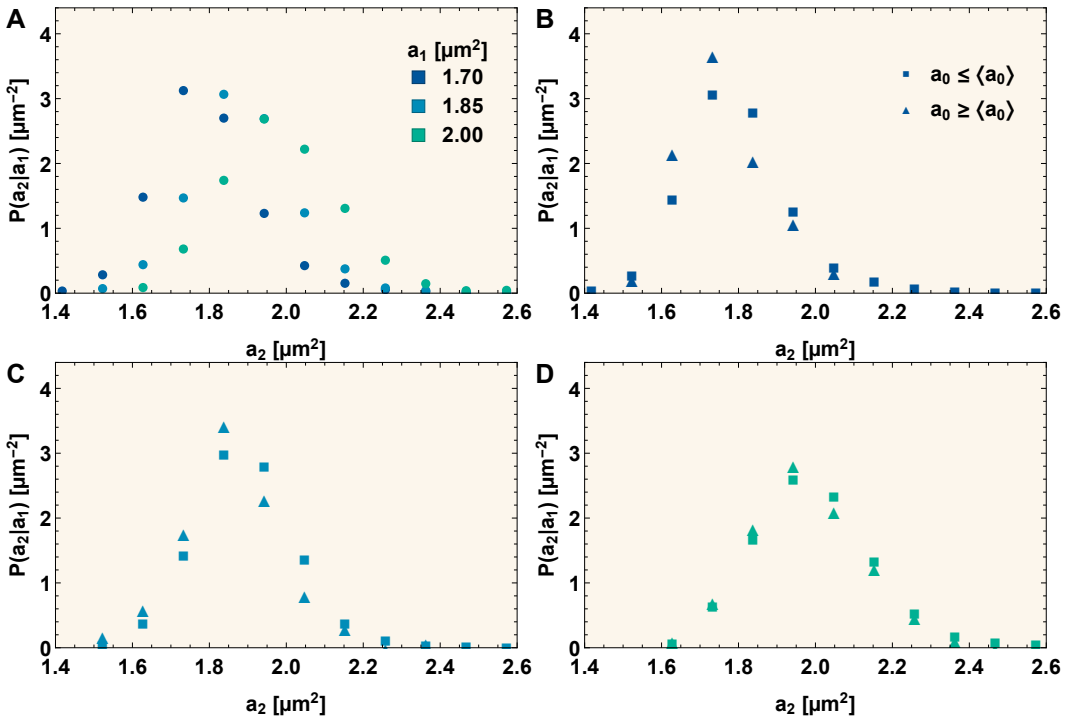

Fig. S7: **Evidence that intergenerational cell size dynamics are Markovian; data taken from balanced growth conditions in complex media.** (**A**) The distributions of the subsequent generation's initial area (a_2) given the current generation's initial area (a_1) are plotted for three different values of a_1. Point colors indicate distinct values of a_1. (**B-D**) For each value of a_1 in (A), the conditional distribution of the subsequent generation's initial area (a_2) given the current generation's initial area (a_1) is further segmented according to whether the previous generation's initial area (a_0) was less than (square) or greater than (triangle) the population mean initial area. The distributions overlap irrespective of whether a_0 was less than or greater than the population mean, indicating that a_2 does not depend on a_0 so long as the value a_1 is fixed. Thus, initial size dynamics are Markovian. Corresponding distributions are provided for minimal media (Fig. S8) and dilute complex media (Fig. S9).

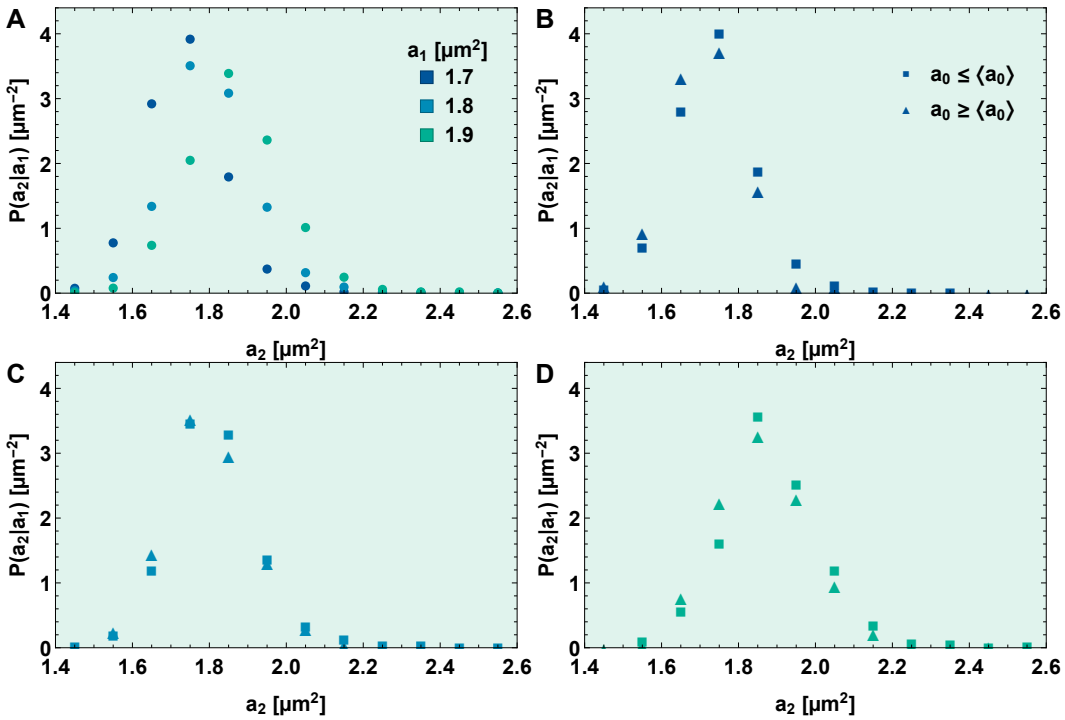

Fig. S8: **Evidence that intergenerational cell size dynamics are Markovian; data taken from balanced growth conditions in minimal media.** (**A**) The distributions of the subsequent generation's initial area (a_2) given the current generation's initial area (a_1) are plotted for three different values of a_1. Point colors indicate distinct values of a_1. (**B-D**) For each value of a_1 in (A), the conditional distribution of the subsequent generation's initial area (a_2) given the current generation's initial area (a_1) is further segmented according to whether the previous generation's initial area (a_0) was less than (square) or greater than (triangle) the population mean initial area. The distributions overlap irrespective of whether a_0 was less than or greater than the population mean, indicating that a_2 does not depend on a_0 so long as the value a_1 is fixed. Thus, initial size dynamics are Markovian. Corresponding distributions are provided for complex media (Fig. S7) and dilute complex media (Fig. S9).

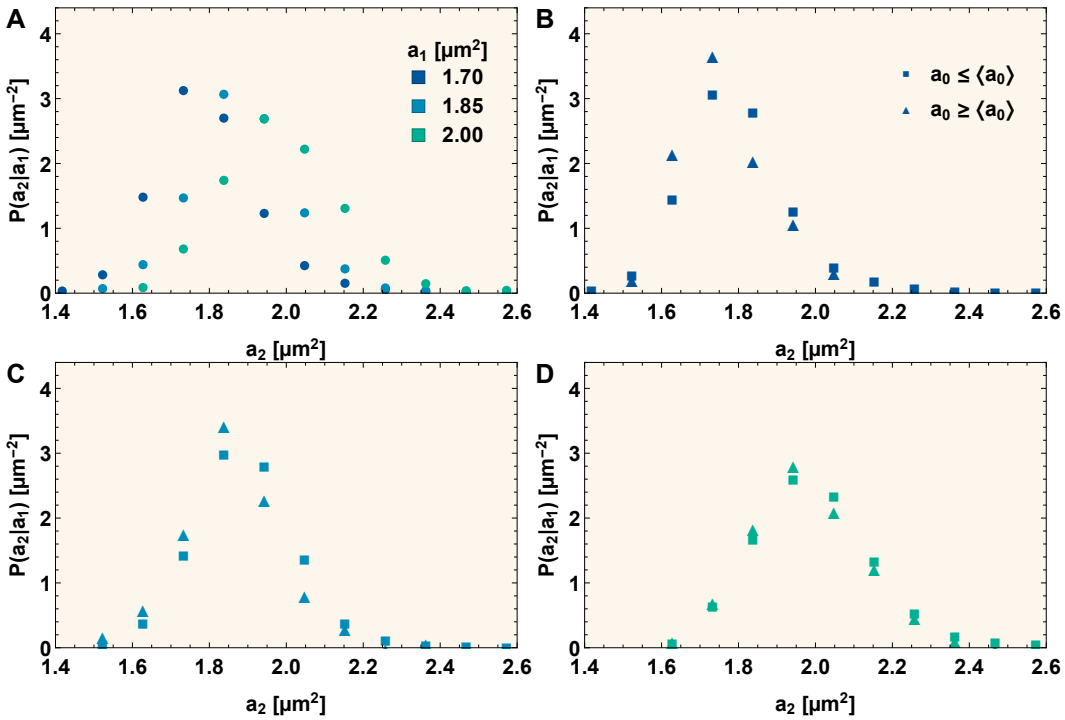

Fig. S9: **Evidence that intergenerational cell size dynamics are Markovian; data taken from balanced growth conditions in dilute complex media.** (**A**) The distributions of the subsequent generation's initial area (a_2) given the current generation's initial area (a_1) are plotted for three different values of a_1. Point colors indicate distinct values of a_1. (**B-D**) For each value of a_1 in (A), the conditional distribution of the subsequent generation's initial area (a_2) given the current generation's initial area (a_1) is further segmented according to whether the previous generation's initial area (a_0) was less than (square) or greater than (triangle) the population mean initial area. The distributions overlap irrespective of whether a_0 was less than or greater than the population mean, indicating that a_2 does not depend on a_0 so long as the value a_1 is fixed. Thus, initial size dynamics are Markovian. Corresponding distributions are provided for complex media (Fig. S7) and minimal media (Fig. S8).

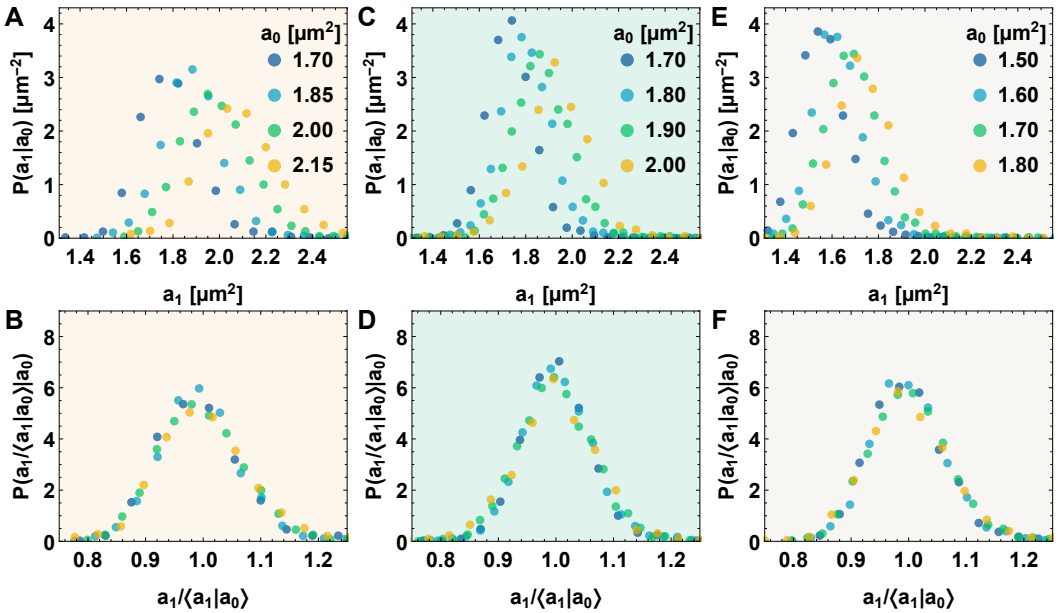

Fig. S10: **Intergenerational scaling: the mean-rescaled distribution of the subsequent generation's initial size, given the current generation's initial size, undergoes a scaling collapse.** The top row shows $P(a_1|a_0)$, the distribution of the subsequent generation's initial size, a_1, pooled by distinct values of the current generation's initial size, a_0. Point colors indicate distinct values of a_0; background colors correspond to different growth media. The bottom row shows corresponding mean-rescaled distributions, with point and background colors as indicated in the top row. Thus, given a growth condition, the two-dimensional function $P(a_1|a_0)$ is constructed from two one-dimensional functions: the mean-rescaled distribution (bottom row), and the a_0-dependent mean $\mu(a_0)$, which sets the calibration curve for how to "stretch" the a_0-independent rescaled distributions (bottom row) to recover the a_0-dependent distributions (top row). Growth conditions are (**A** and **B**) complex media, (**C** and **D**) minimal media, and (**E** and **F**) dilute complex media.

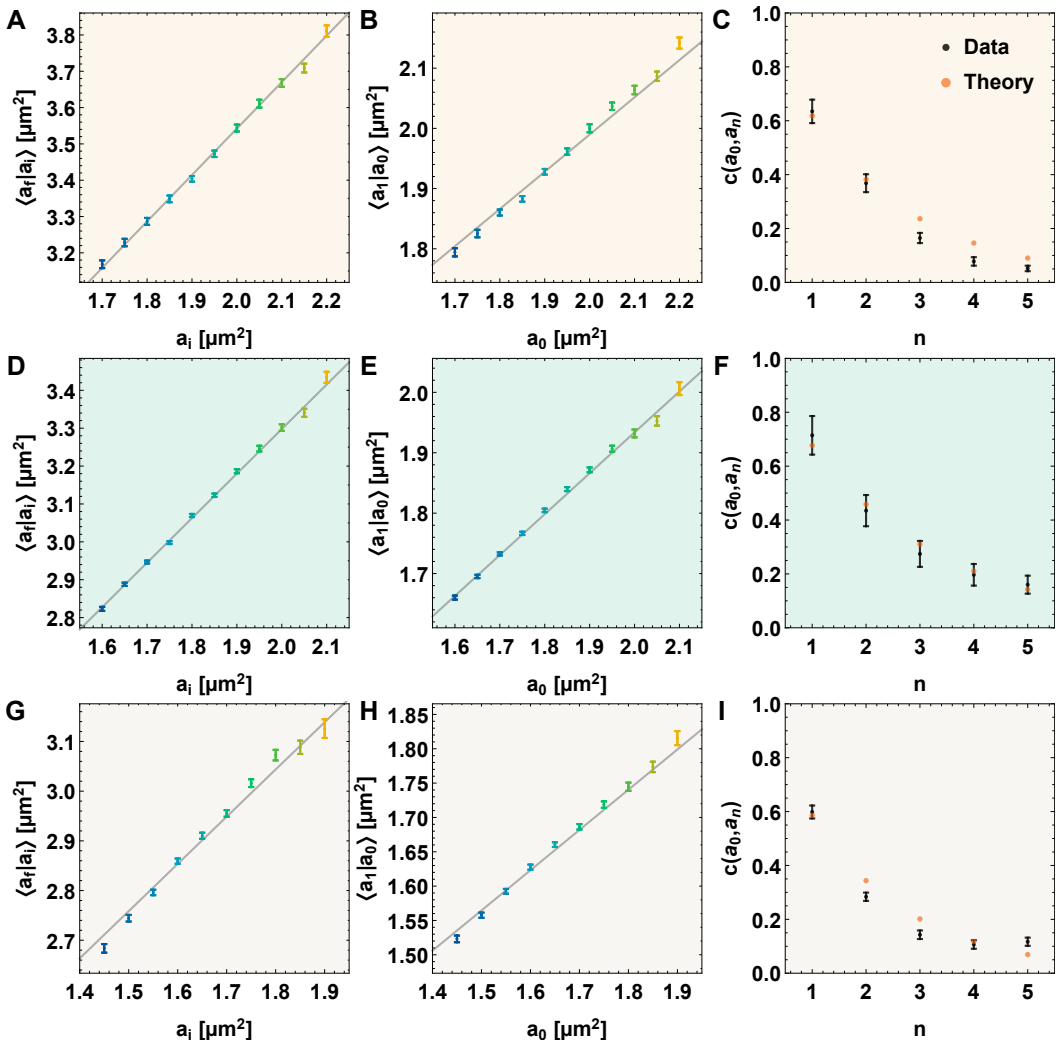

Fig. S11: **Calibration curves that restore the full distribution and generation-by-generation coefficients of correlation in cell sizes.** The left column shows the binned means of final areas plotted for a range of initial areas, along with the linear fit. These calibration curves are used to restore the full conditional final size distributions conditioned on initial size (Figs. 3-A, -C, and -E) from the corresponding mean-rescaled distributions (Figs. 3-B, -D, and -F). The middle column shows the binned means of the next generation's initial areas plotted for a range of the current generation's initial areas, along with the linear fit. These calibration curves are used to restore the full conditional next generation's initial size distributions conditioned on this generation's initial size (Figs. S10-A, -C, and -E) from the corresponding mean-rescaled distributions (Figs. S10-B, -D, and -F). The right column shows the coefficient of correlation between the initial areas in the initial (zeroth) generation and after n consecutive generations for different n. The correlations predicted by our fitting parameter-free theoretical framework (*orange*) closely match those measured from data (*black*). Background colors correspond to different growth media. Growth conditions are (**A-C**) complex media, (**D-F**) minimal media, and (**G-I**) dilute complex media.